

Shaping Causality: Emergence of Nonlocal Light Cones in Long-Range Quantum Systems

Shreyas Sadugol ^{1,*} Giuseppe Luca Celardo,^{2,3,4,†} Fausto Borgonovi,^{5,‡} and Lev Kaplan^{1,§}

¹*Department of Physics, Tulane University, New Orleans, USA*

²*Department of Physics and Astronomy and CSDC, University of Florence, Florence, Italy.*

³*European Laboratory for Non-Linear Spectroscopy (LENS),*

University of Florence, Florence, Italy, 50019 Sesto Fiorentino, Italy

⁴*Istituto Nazionale di Fisica Nucleare (INFN), Sezione di Firenze, 50019 Sesto Fiorentino, Italy.*

⁵*Department of Mathematics and Physics, Catholic University of the Sacred Heart, Milan, Italy*

(Dated: November 27, 2025)

While for non-relativistic short range interactions, the spread of information is local, remaining confined in an effective light cone, long-range interactions can generate either nonlocal (faster-than-ballistic) or local (ballistic) spread of correlations depending on the initial conditions. This makes long-range interactions a rich platform for controlling the spread of information. Here, we derive an effective Hamiltonian analytically and identify the specific interaction term that drives nonlocality in a wide class of long-range spin chains. This allows us to understand the conditions for the emergence of local behaviour in the presence of nonlocal interactions and to identify a regime where the causal space-time landscape can be precisely designed. Indeed, we show that for large long-range interaction strength or large system size, initial conditions can be chosen in a way that allows a local perturbation to generate nonlocal signals at programmable distant positions, which then propagate within effective light cones. The possibility of engineering the emergence of nonlocal Lieb–Robinson–like light cones allows one to shape the causal landscape of long-range interacting systems, with direct applications to quantum information processing devices, quantum memories, error correction, and information transport in programmable quantum simulators.

Keywords: emergent locality, long-range interacting spin systems, cooperative shielding, quantum control

Introduction— Understanding how information and correlations propagate in non-relativistic many-body systems is a central issue for quantum information processing. While non-relativistic quantum systems are not bound to have a finite velocity of information spread, information spread in short-range interacting systems is indeed local as formalized by the Lieb–Robinson bounds [1]. Locality in non-relativistic many body systems refers to the fact that the spread of information can occur at most ballistically within an effective light cone, with a velocity determined by the coupling strength, and with leakage of information outside the light cone being exponentially suppressed. Thus, locality limits information propagation and shapes our understanding of entanglement growth, thermalization, and causality [1–3].

Many programmable quantum platforms including trapped ions [4, 5], Rydberg atom arrays [6], and dipolar molecules [7] realize long-range couplings of the form $J_{ij} \sim J_{\text{long}}/|i - j|^\alpha$ for one component of the spin, which we take without loss of generality to be the x -component. Such interactions can permit faster-than-ballistic spread, suggesting a breakdown of locality [3, 4, 8].

Interestingly, several studies have shown that long-range interactions may sometimes fail to enhance propagation [9–20], and [21, 22] introduced the notion of *cooperative shielding*, wherein emergent approximate superselection rules dynamically isolate (shield) certain subspaces from long-range couplings up to time scales that grow with system size (cooperativity), effectively sup-

pressing nonlocal propagation. Some consequences of cooperative shielding have been confirmed experimentally [16]. This paradoxical behaviour of long-range interacting systems is due to the fact that information spread strongly depends on initial conditions. Despite these advances, a clear microscopic understanding, for generic interaction range, of when and why locality can emerge from nonlocal interactions, has remained elusive for nearly a decade.

Here we analyze a class of long-range interacting spin systems and resolve this problem by mapping the spin Hamiltonian into a hard boson Hamiltonian in which the terms leading to nonlocal behaviour are explicitly isolated. This allows us to determine the regime parameters and the initial conditions for which nonlocal effects are small (yielding strictly Lieb–Robinson-like dynamics) and also to elucidate how long-range interacting systems can be exploited to gain precise control of information spread in a wide class of non-relativistic many-body spin systems. Our approach connects naturally to the Zeno Hamiltonian introduced in Ref. [21] via band projection.

Our analysis reveals how local and nonlocal behaviors arise directly from the initial conditions. In the large system size limit, for a given number of excitations (number of up spins along the direction identified by the anisotropic long-range interaction), any change in the initial configuration generates signals around each excitation that spread within light cones of identical velocities. If all excitations are confined to a finite region, nonlo-

cal effects remain also restricted to that region, leaving the dynamics outside it entirely local despite strong long-range interactions. Within each causal region, our theory predicts the precise pattern and strength of nonlocal signal spread, enabling deterministic control of information flow through the choice of initial conditions. For instance, by choosing the position of the excitation, we can obtain immediate but fully controllable signal propagation at precise positions. Long-range interactions are essential for this control, while short-range systems lack such tunability, as their dynamics are always locally constrained.

This provides a controlled route to engineer locality from nonlocal interactions, unifying prior observations [21, 22] and offering an experimentally accessible framework for robust quantum memories, error correction, and transport.

Model— We study a 1D spin- $\frac{1}{2}$ chain of length N governed by

$$\hat{H} = \sum_{j=1}^{N-1} J_z \sigma_j^z \sigma_{j+1}^z + \sum_{i < j} \frac{J_x}{|j-i|^\alpha} \sigma_i^x \sigma_j^x, \quad (1)$$

where α controls the interaction range, interpolating between infinite-range ($\alpha = 0$) and nearest-neighbor ($\alpha \rightarrow \infty$) limits. We also apply the standard Kac rescaling [23–25]

$$J_x = \frac{J_{\text{long}}}{\mathcal{N}_{\text{Kac}}(\alpha, N)}, \quad \mathcal{N}_{\text{Kac}}(\alpha, N) = \frac{1}{N} \sum_{i < j} \frac{1}{|i-j|^\alpha},$$

so that the energy per site remains finite in the thermodynamic limit. For $\alpha = 0$, this reduces to $J_x \simeq 2J_{\text{long}}/N$. Throughout this paper, fixing J_{long} corresponds to applying Kac rescaling, since J_x is rescaled accordingly, whereas fixing J_x implies no Kac rescaling.

Band structure— When $J_{\text{long}} \gg J_z$, the dynamics are dominated by the long-range $\sigma_i^x \sigma_j^x$ interaction. For $\alpha = 0$, this term depends only on the total x -magnetization $M_x = \frac{1}{2} \sum_{j=1}^N \sigma_j^x$, so the spectrum organizes into well-separated ‘‘bands’’ (or excitation manifolds) labeled by the number $b = 0, 1, 2, \dots$ of spins aligned along $+x$. The band energies E_b are quadratic in b with large interband gaps ΔE_b that strongly suppress transitions between them. Explicitly, one has:

$$E_b = \frac{J_x}{2}(N-2b)^2 - \frac{J_x N}{2}, \quad (2)$$

$$\begin{aligned} \Delta E_b &= E_b - E_{b-1} = -2J_x(N-2b-1) \\ &= -4J_{\text{long}}(1-2b/N-1/N). \end{aligned} \quad (3)$$

The subleading Ising term J_z couples only bands $b \leftrightarrow b \pm 2$. In leading-order perturbation theory, the interband leakage probability scales as $P_{\text{leave}} \sim (J_z/J_{\text{long}})^2$, thus vanishing in the $J_{\text{long}} \gg J_z$ regime [21, 26].

Effective Hamiltonian— The system can be mapped to a model of hard-core bosons hopping on a lattice of

size N , where boson occupation corresponds to spin in the σ^x basis, Eq. (4). This mapping provides a natural framework for analyzing emergent locality. In the Supplemental Material Secs. B, D two independent but equivalent derivations are presented: one via Holstein-Primakoff transformations and spin-wave theory, and the other via an exact subspace projection onto the fixed-excitation manifold. Explicitly, Eq. (1) takes the form of a bosonic Hamiltonian, which is equivalent to the full spin Hamiltonian Eq. 1:

$$\begin{aligned} \hat{H}_{\text{eff}} &= J_z \sum_i (\hat{a}_i^\dagger \hat{a}_{i-1} + \hat{a}_{i-1}^\dagger \hat{a}_i) + J_z \sum_i (\hat{a}_i^\dagger \hat{a}_{i-1}^\dagger + \hat{a}_i \hat{a}_{i-1}) \\ &+ \sum_i V(i) \hat{n}_i + \sum_{i < j} W(i, j) \hat{n}_i \hat{n}_j + U \sum_i \hat{n}_i (\hat{n}_i - 1) + E_{b=0} \end{aligned} \quad (4)$$

with

$$\begin{aligned} V(i) &= -2J_x \sum_{j \neq i} \frac{1}{|i-j|^\alpha}, & W(i, j) &= \frac{4J_x}{|i-j|^\alpha}, \\ U \rightarrow \infty & \text{(hard-core),} & E_{b=0} &= J_x \sum_{i < j} \frac{1}{|i-j|^\alpha}. \end{aligned}$$

In this representation, the band number b becomes the total boson occupation number $\sum_i \hat{n}_i$, and the second term in \hat{H}_{eff} contains the coupling between bands. For large long-range coupling J_x , the transition probability between bands scales as J_z^2/J_x^2 , and projection onto a single band becomes an increasingly accurate description of the physics [21]. Manifestly, the only source of nonlocality in \hat{H}_{eff} is the two-body interaction $W(i, j) \propto 1/|i-j|^\alpha$.

For $0 < \alpha < 1$, the many-body bands remain, but intraband degeneracies lift. For band 1, the band width δE_1 is set by the energy difference between excitations at the chain center and edge, arising from the V term in Eq. (4), and for small α we have (see Sec. C in the Supplemental Material)

$$\frac{\delta E_1}{|\Delta E_1|} \sim \frac{2J_x(\ln 2)\alpha N^{1-\alpha}}{2J_x N^{1-\alpha}} = (\ln 2)\alpha. \quad (5)$$

As $\alpha \rightarrow 1$, the ratio becomes $\mathcal{O}(1)$; for $\alpha > 1$ the band width exceeds the gap, causing spectral overlap and interband mixing. Since higher bands broaden by an additional factor $\sim b$, the overlap criterion for band 1 already determines the onset of overlap for the full spectrum.

Method— To probe the emergence of locality, we propagate states that are typically initialized in the same manifold but differ at one or more sites, and then track the Frobenius-norm distance, defined below between the two reduced density matrices outside the region of the initial perturbation. Unlike two-point correlators, OTOCs, or magnetization, which test specific observables in specific orientations, the Frobenius norm in Eq. (10) captures the maximum possible change in any measurement

outcome, making it sensitive to coherent differences that other probes can miss.

Specifically, we start with two states

$$|\psi_a\rangle = \frac{1}{\sqrt{2}} (|\psi_1\rangle + |\psi_2\rangle), \quad (6)$$

$$|\psi_b\rangle = \cos\left(\frac{\pi}{4} + \epsilon\right) |\psi_1\rangle + \sin\left(\frac{\pi}{4} + \epsilon\right) |\psi_2\rangle, \quad (7)$$

that differ only by a small coherent rotation $\epsilon \ll 1$ ($\epsilon = 0.01$ in simulations) on the Bloch sphere. Note that $|\psi_a\rangle - |\psi_b\rangle \sim |\psi_1\rangle - |\psi_2\rangle$, so when the difference between $|\psi_1\rangle$ and $|\psi_2\rangle$ is local, the (infinitesimal) difference between $|\psi_a\rangle$ and $|\psi_b\rangle$ is also local. Initial basis states $|\psi_1\rangle$ and $|\psi_2\rangle$ are chosen within a fixed-excitation manifold to avoid artifacts from comparing states in different manifolds (which will be discussed in [26]). Here an excitation is a spin pointing upwards in the direction identified by the anisotropy of the long-range interaction (the x -direction in our case). In the following, we will be interested in the scenario where $|\psi_1\rangle$ and $|\psi_2\rangle$, and therefore also $|\psi_a\rangle$ and $|\psi_b\rangle$, differ by moving one excitation. For example, in the two-excitation ($b = 2$) manifold, we may choose

$$|\psi_1\rangle = |\downarrow\uparrow\downarrow\uparrow\downarrow\downarrow\cdots\downarrow\rangle, \quad |\psi_2\rangle = |\downarrow\downarrow\uparrow\uparrow\downarrow\downarrow\cdots\downarrow\rangle, \quad (8)$$

where $|\psi_1\rangle$ has spin flips at sites 2 and 4 and $|\psi_2\rangle$ has spin flips at sites 3 and 4 in the σ^x basis, and we may label this pair of initial states as $(2, 4; 3, 4)$. More generally, $|\psi_1\rangle$ may have spin flips at sites i_1 and i_2 , and $|\psi_2\rangle$ may have spin flips at j_1 and j_2 in the σ^x basis, and this scenario may be labeled

$$(i_1, i_2; j_1, j_2) \equiv (|\psi_1(i_1, i_2)\rangle, |\psi_2(j_1, j_2)\rangle). \quad (9)$$

To minimize boundary effects, initial flips (excitations) are chosen away from the chain boundaries. We compute the Frobenius norm of the difference between the two reduced density matrices at each site n :

$$\|\Delta\rho_n(t)\|_F = \sqrt{\text{Tr}(\Delta\rho_n \Delta\rho_n^\dagger)}, \quad (10)$$

where $\rho_n^{(a)}$, $\rho_n^{(b)}$ are the local reduced density operators at the n^{th} site for states evolved from $|\psi_a\rangle$ and $|\psi_b\rangle$, respectively, and $\Delta\rho_n = \rho_n^{(1)} - \rho_n^{(2)}$. Other norms (including the trace norm and other Schatten p -norms) yield equivalent qualitative behaviour in our tests. The Frobenius norm is used for computational efficiency.

Throughout this work, we use a normalized Frobenius norm, obtained by dividing $\|\Delta\rho_n(t)\|_F$ by its global maximum over all sites and times, which maps all signals to the interval $[0, 1]$. For brevity, we use the term ‘‘Frobenius norm’’ to refer to this normalized quantity. Open boundary conditions and Kac rescaling are applied unless stated otherwise. We set $J_z = 1$ without loss of generality, since the dynamics depend only on the J_{long}/J_z ratio. The light-cone boundary is obtained from first-arrival times,

which are the earliest times at which $\|\Delta\rho_n(t)\|_F = 0.01$, fitted to a straight line. The outside-the-cone profile is extracted at a fixed time slice by locating the crest of the wave propagating outward from the perturbation and fitting the decay of $\|\Delta\rho_n(t)\|_F$ beyond the wave crest (see insets of Fig. 1). \hat{H}_{eff} is the effective Hamiltonian (4), which is equivalent to the full Hamiltonian in Eq. (1), and \hat{H}_{eff}^b is the effective Hamiltonian projected on band b (without interband coupling).

Results: Emergence of locality and role of nonlocal term W — To probe the emergence of locality, we first evolve initial states in band $b = 1$ using Hamiltonian (1). As J_{long} increases, two key features appear: (i) non-local signals outside the light cone are suppressed, and (ii) the light-cone velocity grows and then saturates. A detailed analysis of the information spread velocity versus J_{long} and α will appear elsewhere [26], showing that the velocity is α -independent for $\alpha < 1$ and saturates for $J_{\text{long}} > J_z$. Here, we focus on (i). For small J_{long} , significant signal appears outside the light cone; increasing J_{long} suppresses this nonlocality, as shown in Fig. 1. The signal outside the cone drops super-exponentially, consistent with the Lieb-Robinson bound [1].

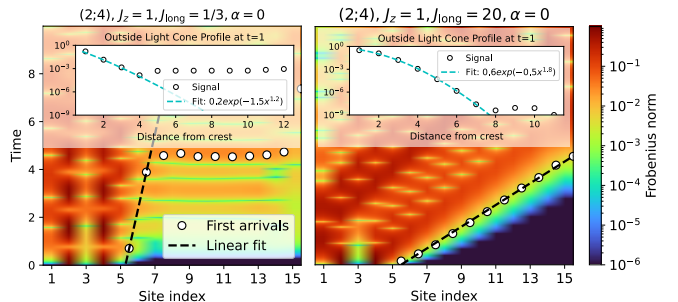


FIG. 1. Density plots of the Frobenius norm showing light-cone dynamics under the full Hamiltonian (1) with initial states prepared in band $b = 1$: $(2; 4)$ (notation defined in Eq. (9)). At weaker long-range coupling ($J_{\text{long}} = 1/3$, left), the nonlocal signal outside the light cone is strong, while at stronger long-range coupling ($J_{\text{long}} = 20$, right), locality emerges. The threshold for first arrival times is 0.01. In both cases we fix $N = 15$ and $\alpha = 0$. Here and throughout we set $J_z = 1$. The insets show outside-the-cone profiles at time $t = 1$.

The sole nonlocal term in the long-range Hamiltonian (4) is $W = \sum_{i < j} W(i, j) \hat{n}_i \hat{n}_j$. (For large α , this term also becomes local, and in the $\alpha \rightarrow \infty$ limit the system reduces to the integrable nearest-neighbor XY model chain with exactly local dispersion [26].) Eliminating the W term restores strictly local light cones across all excitation manifolds, values of α , and ratios J_x/J_z (See Fig. S8 for more comprehensive results). If we instead start with spins polarized along the z direction (corresponding to an initial state spread out over all bands in the spin- x basis), nonlocality appears also for large J_x/J_z , but once again

exact locality is restored when the W term is subtracted from the Hamiltonian (Fig. 2). Thus, for any parameter values, W alone drives light-cone violation.

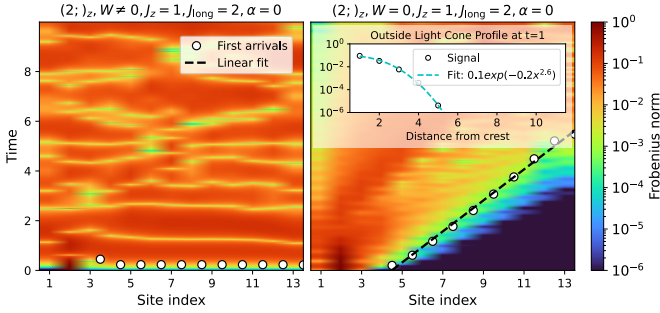


FIG. 2. Density plots of the Frobenius norm showing light-cone dynamics under the full Hamiltonian (1) with $|\uparrow_z, \downarrow_z, \dots\rangle$ and $|\uparrow_z, \uparrow_z, \uparrow_z, \dots\rangle$ as the two initial states being compared. Here $N = 13$, $J_{\text{long}} = 2$, and $\alpha = 0$. Instantaneous propagation of the perturbation to large distances occurs for the full Hamiltonian (left), while removing W restores a strict Lieb-Robinson-local light cone (right). Nonlocality originates from W . The inset shows the outside-the-cone profile at time $t = 1$.

From the W term, two distinct processes emerge naturally. The *intraband* contribution corresponds to a first-order process in the W term, acting entirely within a given excitation manifold. In contrast, the *interband* contribution to nonlocality arises from the interplay between the W term and virtual transitions between manifolds via J_z . We will first study the scaling of the intraband nonlocality by projecting onto a single band, and then proceed to analyze the scaling of the interband nonlocality.

Projecting onto a single band: *Probing intraband nonlocality*— For single-excitation states in band $b = 1$, the effective Hamiltonian (4) reduces to

$$\hat{H}_{\text{eff}}^{b=1} = J_z \sum_j (|j\rangle\langle j+1| + \text{h.c.}) - 2J_{\text{long}} \sum_j \epsilon_j |j\rangle\langle j|, \quad (11)$$

which is a strictly local tight-binding model (see also Supplemental Material Sec. D). All two-body W terms vanish identically. Thus, while the full Hamiltonian exhibits locality only above a finite signal threshold ($\sim 10^{-3}$ in the inset of Fig. 1, left panel), the projected Hamiltonian $\hat{H}_{\text{eff}}^{b=1}$ is strictly Lieb–Robinson local for all α and J_{long}/J_z (see Fig. S1). The strict locality of the single-band Hamiltonian $\hat{H}_{\text{eff}}^{b=1}$ explains why approximate locality is observed for the full Hamiltonian in the shielding regime (large J_{long}/J_z) [21, 26] when the system is initialized in band $b = 1$ as in Fig. 1.

Single band with $\alpha = 0$: For initial states in band $b > 1$, the intraband term $W = \binom{b}{2} \cdot 4J_x = 2J_x b(b-1)$ contributes only a constant spectral shift. The projected Hamiltonian is therefore strictly local, as verified for band 3 in the Supplemental Material in Fig. S4 (Panel a). More generally, for $\alpha = 0$ any single-band projection

yields local dynamics.

Single band with $0 < \alpha < 1$: For band $b > 1$ with finite α , the degeneracy of the W term within the band is broken, and we have a residual nonlocal contribution within the W term, given by a sum over all pairs of excitations (see (4)). At leading order in perturbation theory, the Frobenius norm signal is given by the variance of this term, which scales as (see Fig. S2)

$$\|\Delta\rho_n(t)\|_F^{\text{intraband}} \sim \langle \Delta W^2 \rangle \sim \frac{f(\alpha)g(b)J_{\text{long}}^2}{N^{2(1-\alpha)}}, \quad (12)$$

where the variance is taken over the $\binom{N}{b}$ states in band b , $g(b)$ takes into account the summation over $\binom{b}{2}$ terms in the W term for band b , and $f(\alpha) \sim \alpha^2$ for small α . Note that without Kac rescaling, Eq. (12) becomes independent of N .

In order to analyze the spread of information in finite systems, it is convenient to consider two different kinds of initial conditions: *i*) *close* configurations, where all excitations are confined in a small region compared to the chain length, allowing us to analyze what happens far away from the region where the excitations are present; and *ii*) *far* configurations, where the distance between excitations is comparable to the chain length, enabling us to analyze what happens inside the region where the excitations are present. In the $b = 2$ manifold, the nonlocal W term can be isolated by comparing states that share one of two excitations, i.e., $(i, j; k, j)$. In Fig. 3 (left), the *close* configuration $(2, 4; 3, 4)$ places the common j^{th} excitation near i and k , and no nonlocal signal is observed since all two-body interactions remain within the light cone. In contrast, in the *far* configuration $(2, 28; 3, 28)$, the $j = 28$ excitation lies well outside the light cone originating from the vicinity of sites 2 and 3. Here, the difference between the interactions of pairs $(2, 28)$ and $(3, 28)$ results in a nonlocal signal near site 28 when comparing the propagation of these two initial states.

Thus, the effect of the W term within a band is *conditionally* nonlocal: genuine nonlocal effects appear in the *far* case, when the initial state contains another excitation that lies outside the causal region of the excitation that is being varied or perturbed. See Figs. S3, S4, S5, and S6 in the Supplemental Material for illustrations of the nonlocal behaviour in the *far* case. In particular, Fig. S6 shows that the nonlocal signal gets weaker, as theoretically expected, in the thermodynamic limit $N \rightarrow \infty$ with Kac prescription.

We also emphasize that for large α , this behavior disappears (Fig. 6, panel a): information about the initial perturbation at sites 2 and 3 always remains confined within the causal light cone and reaches other sites only after a time proportional to their distance, preserving locality. One does not observe a second signal of the kind that is shown in the other panels.

Coupling all bands— Accessing interband nonlocality, induced by the interplay of the W term with inter-

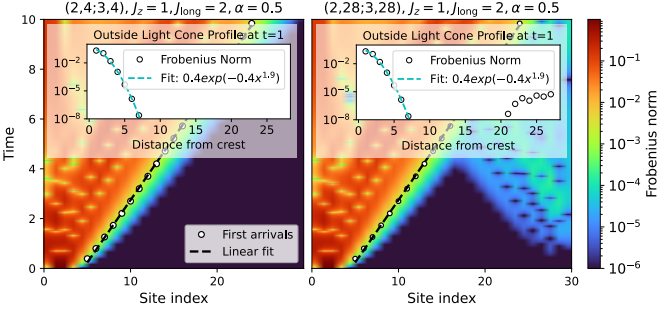


FIG. 3. Density plots of the Frobenius norm showing light-cone dynamics under the projected Hamiltonian $\hat{H}_{\text{eff}}^{b=2}$ with initial states prepared in band $b = 2$ for $\alpha = 0.5$ and $J_{\text{long}}/J_z = 2$. In the *close* configuration (2, 4; 3, 4) (left) (notation defined in Eq. (9)), the additional excitation at site 4 lies within the light cone (except at very short times), and no detectable nonlocal signal is observed outside. In the *far* configuration (2, 28; 3, 28) (right), the additional excitation at site 28 lies outside the light cone of the excitation, and a relatively weak but clear nonlocal signal appears showing conditional nonlocality from W interactions. The insets show outside-the-cone profiles at $t = 1$.

band transitions, requires coupling across all bands. In general, this interband nonlocality coexists with the intraband nonlocality that is already present when dynamics is restricted to a single band, as discussed above. At $\alpha = 0$, however, we have seen that intraband nonlocality vanishes identically, so any residual nonlocal signal must stem from higher-order interband processes. The $\alpha = 0$ limit therefore provides a clean setting to isolate and characterize interband nonlocality. Numerically, we find that the nonlocal signal scales as

$$\|\Delta\rho_n(t)\|_F^{\text{interband}} \sim J_{\text{long}}^{-\gamma(b,N)} N^{-\delta(b,N)} \lesssim J_{\text{long}}^{-2} N^{-2}, \quad (13)$$

as illustrated in Fig. 4. The exponents $\gamma(b, N), \delta(b, N)$ depend nontrivially on b and N , but never fall below 2; all cases decay faster than this bound. As in the case of intraband nonlocality (Eq. (12)), we see that the signal from interband nonlocality approaches 0 for large N .

For finite α , both intra- and interband nonlocality contributions are present, but they can be distinguished using different initial state configurations. In the *close* configuration, intraband contributions are suppressed (once the light cone expands to include all initial excitations), and any residual nonlocal signal must originate from interband effects. By contrast, in the *far* configuration, intraband contributions are active, competing with the weaker interband term. Figure 5 illustrates this distinction: in the *far* case, the intraband scaling of Eq. (12) dominates, establishing that intraband effects provide the leading contributions to nonlocality both for large J_{long} and large N .

Control of nonlocality— Figure 6 highlights a striking feature of the class of long-range interacting systems an-

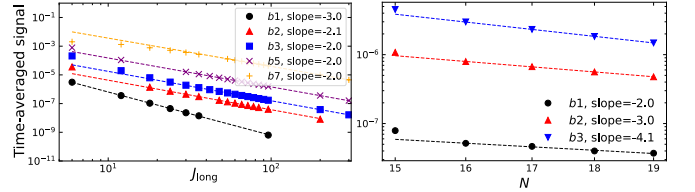


FIG. 4. Time-averaged Frobenius norm for dynamics under the full Hamiltonian for $t \in [0, 2]$ at site 13 for the *close* configuration, probing the interband nonlocal signal at $\alpha = 0$. The expected scaling is $\|\Delta\rho_n(t)\|_F^{\text{interband}} \lesssim J_{\text{long}}^{-2} N^{-2}$. Left: dependence on J_{long} for fixed $N = 15$ and initial states in different bands (notation defined in Eq. (9)): $b = 1$: (2; 3), $b = 2$: (2, 5; 3, 5), $b = 3$: (2, 5, 7; 3, 5, 7), $b = 5$: (2, 5, 7, 9, 11; 3, 5, 7, 9, 11), and $b = 7$: (2, 5, 7, 9, 11, 13, 15; 3, 5, 7, 9, 11, 13, 15). Right: dependence on system size N at fixed $J_{\text{long}} = 20$. Without Kac rescaling, the nonlocal signal would decay even faster with N . Data points show simulation results; dashed lines are fits.

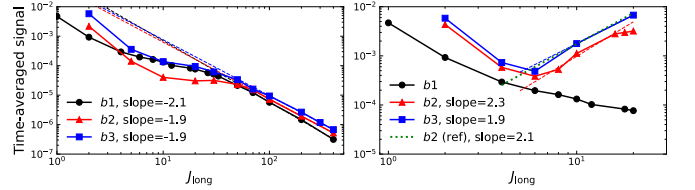


FIG. 5. Time-averaged Frobenius norm for dynamics under the full Hamiltonian, for $t \in [0, 2]$ at site 13 as a function of J_{long} shows competing scaling of intra- and interband nonlocalities at $\alpha = 0.5$ and $N = 15$. Left: *Close* configurations, where intraband nonlocality is suppressed and the residual signal isolates interband effects (bands $b = 1$: (2; 3), $b = 2$: (2, 5; 3, 5), $b = 3$: (2, 5, 7; 3, 5, 7)). Right: *Far* configurations at the same parameters (bands $b = 2$: (2, 13; 3, 13) and $b = 3$: (2, 11, 13; 3, 11, 13)), where intraband nonlocality asymptotically dominates over interband effects. For reference, the intraband signal of band $b = 2$ is taken from Fig. S2 in the Supplemental Material. Intraband N -scaling only emerges for large N ; for small chains, the competition between the two terms masks any clear scaling.

alyzed here. The two-body term $W(i, j)$ couples every pair of excitations; when one excitation is perturbed, a light cone appears at every other excitation. The light cones caused by this two-body nonlocal effect evolve independently of one another. This demonstrates that nonlocality can be precisely controlled, enabling the creation of independent, non-interacting propagation channels.

Conclusion— Emergence of locality: We have extended the understanding of the cooperative shielding mechanism [21, 22], showing that emergent locality in long-range interacting systems originates from dynamics confined to excitation manifolds for $\alpha < 1$. Within the $b = 1$ (single-excitation) manifold, the effective Hamiltonian is strictly Lieb–Robinson local. For band $b > 1$, two distinct processes govern nonlocal behavior. (i) *Interband* nonlocality arises due to couplings between ex-

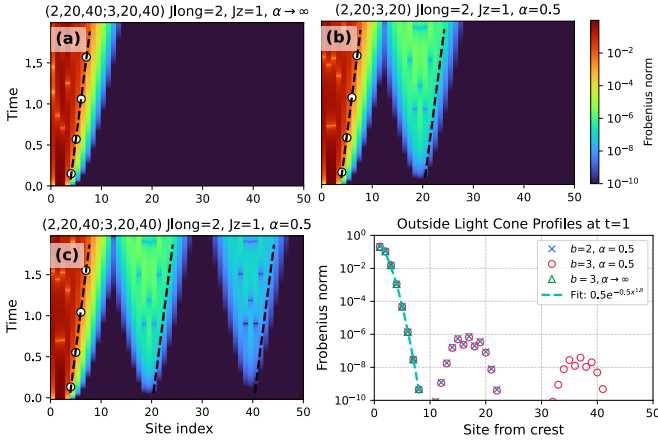


FIG. 6. Density plots of the Frobenius norm showing light-cone dynamics under the band-projected Hamiltonian \hat{H}_{eff}^b , which the full Hamiltonian effectively converges to in the large J_{long} limit. Panels a,c: Evolution with $\hat{H}_{\text{eff}}^{b=3}$ for initial states prepared band 3: $(2,20,40;3,20,40)$ (notation defined in Eq. (9)), for $\alpha \rightarrow \infty$ and $\alpha = 0.5$ respectively. Panel b: Evolution with $\hat{H}_{\text{eff}}^{b=2}$ for initial states in band 2: $(2,20;3,20)$. Here $J_{\text{long}} = 2$ and $N = 100$ (only 50 sites shown). As expected, in panel c, the light cone in the middle is independent of the light cone on the right. In panel a, no secondary light cones are visible since the Hamiltonian is nearest-neighbor. These results can also be recreated using experimentally accessible observables as shown in Figs. S10 and S11. This allows for precise control of information by varying J_{long} , α , and the distance between excitations. (See Figs. S3, S4, and S5 respectively.) Such versatility cannot be achieved using short-ranged Hamiltonians (panel a).

citation manifolds. This vanishes in the large- N thermodynamic limit and also in the limit of large- J_{long} (strong long-range coupling), both with and without Kac prescription. (ii) *Intraband* nonlocality arises from the two-body W interaction, which induces correlations between distant sites within a fixed manifold. This effect increases with long range interaction strength.

The nonlocal effect strongly depends on initial conditions. Indeed, if all initial excitations remain confined to a finite region, then nonlocal effects remain relevant as we increase the system size only in the region where the excitations are present, while outside it, the signal decays exponentially with the distance. Inside the region containing the excitations, without Kac rescaling, this contribution persists for $0 < \alpha < 1$ in the large- N limit, while it vanishes with Kac rescaling, restoring complete Lieb–Robinson locality in the thermodynamic limit. In an intermediate- N regime with large J_{long} , interband nonlocality is already suppressed while intraband correlations remain finite.

Control: The regime where intraband nonlocality dominates (large N or large J_{long}) enables direct control of nonlocality. By tuning N , J_{long} , and the spatial arrangement of the initial excitations, one can precisely program

when and where information arrives and with what amplitude. The surviving intraband correlations are non-interacting and propagate through Lieb–Robinson-like local dynamics governed by the local coupling scale J_z . (See Figs. S12 and S13 in the Supplemental Material.)

Such controllable, quasi-local propagation establishes cooperative shielding as a new route to engineer robust transport and stable quantum memories, providing a microscopic foundation for emergent locality and causal dynamics in globally interacting many-body quantum systems [27].

* ssadugol@tulane.edu

† giuseppelucca.celardo@unifi.it

‡ fausto.borgonovi@unicatt.it

§ lkaplan@tulane.edu

- [1] E. H. Lieb and D. W. Robinson, Comm. Math. Phys. **28**, 251 (1972).
- [2] M. B. Hastings and T. Koma, Comm. Math. Phys. **265**, 781–804 (2006).
- [3] M. C. Tran, A. Y. Guo, C. L. Baldwin, A. Ehrenberg, A. V. Gorshkov, and A. Lucas, Phys. Rev. Lett. **127**, 160401 (2021).
- [4] P. Jurcevic, B. P. Lanyon, P. Hauke, C. Hempel, P. Zoller, R. Blatt, and C. F. Roos, Nature **511**, 202 (2014), arXiv:1401.5387 [quant-ph].
- [5] C. Monroe, W. C. Campbell, L.-M. Duan, Z.-X. Gong, A. V. Gorshkov, P. W. Hess, R. Islam, K. Kim, N. M. Linke, G. Pagano, P. Richerme, C. Senko, and N. Y. Yao, Rev. Mod. Phys. **93**, 025001 (2021).
- [6] A. Browaeys and T. Lahaye, Nature Physics **16**, 132 (2020).
- [7] B. Yan, S. A. Moses, B. Gadway, J. P. Covey, K. R. A. Hazzard, A. M. Rey, D. S. Jin, and J. Ye, Nature **501**, 521 (2013).
- [8] P. Richerme, Z.-X. Gong, A. Lee, C. Senko, J. Smith, M. Foss-Feig, S. Michalakis, A. V. Gorshkov, and C. Monroe, Nature **511**, 198 (2014).
- [9] L. Cevolani, G. Carleo, and L. Sanchez-Palencia, Phys. Rev. A **92**, 041603 (2015).
- [10] Z.-X. Gong, M. Foss-Feig, S. Michalakis, and A. V. Gorshkov, Phys. Rev. Lett. **113**, 030602 (2014).
- [11] T. Kuwahara and K. Saito, Phys. Rev. X **10**, 031010 (2020).
- [12] D. J. Luitz and Y. Bar Lev, Phys. Rev. A **99**, 010105 (2019).
- [13] M. Foss-Feig, Z.-X. Gong, C. W. Clark, and A. V. Gorshkov, Phys. Rev. Lett. **114**, 157201 (2015).
- [14] D. Arrufat-Vicente and N. Defenu, Freezing and shielding under global quenches for long-range interacting many-body systems (2024), arXiv:2407.06072 [quant-ph].
- [15] P. Azodi and H. A. Rabitz, Emergence of light cones in long-range interacting spin chains is due to destructive interference (2025), arXiv:2407.11639 [quant-ph].
- [16] W. Tan, P. Becker, F. Liu, G. Pagano, K. Collins, A. De, L. Feng, H. Kaplan, A. Kyprianidis, R. Lundgren, W. Morong, S. Whitsitt, A. Gorshkov, and C. Monroe, Nature Physics **17**, 742 (2021).
- [17] P. P. Mazza, G. Perfetto, A. Leroose, M. Collura, and

- A. Gambassi, Physical Review B **99**, 180302(R) (2019).
- [18] M. Kormos, M. Collura, G. Takács, and P. Calabrese, Nature Physics **13**, 246 (2017).
- [19] N. Defenu, T. Donner, T. Macrì, G. Pagano, S. Ruffo, and A. Trombettoni, Rev. Mod. Phys. **95**, 035002 (2023).
- [20] N. Defenu, A. Lerose, and S. Pappalardi, Phys. Rep. **1074**, 1 (2024).
- [21] L. F. Santos, F. Borgonovi, and G. L. Celardo, Phys. Rev. Lett. **116**, 250402 (2016).
- [22] G. L. Celardo, R. Kaiser, and F. Borgonovi, Phys. Rev. B **94**, 144206 (2016).
- [23] T. Botzung, D. Hagenmüller, G. Masella, J. Dubail, N. Defenu, A. Trombettoni, and G. Pupillo, Phys. Rev. B **103**, 155139 (2021).
- [24] T. Mori, Phys. Rev. E **86**, 021132 (2012).
- [25] M. Kastner, Long-range systems, (non)extensivity, and the rescaling of energies (2025), arXiv:2506.22296 [cond-mat.stat-mech].
- [26] S. Sadugol, G. L. Celardo, F. Borgonovi, and L. Kaplan, Dynamics and shielding in many-body systems (2025), link to preprint will be inserted once published.
- [27] S. Ausilio, F. Borgonovi, G. L. Celardo, J. Y. Malo, and M. L. Chiofalo, Memory preservation and cooperative shielding in complex quantum networks (2025), arXiv:2503.05655 [quant-ph].

Supplemental Materials: Shaping Causality: Emergence of Nonlocal Light Cones in Long-Range Quantum Systems

A. Conventions

Throughout this work, we use a normalized Frobenius norm, obtained by dividing $\|\Delta\rho_n(t)\|_F$ by its global maximum over all sites and times, which maps all signals to the interval $[0, 1]$. For brevity, we use the term “Frobenius norm” to refer to this normalized quantity.

Open boundary conditions and Kac rescaling are applied unless stated otherwise. We set $J_z = 1$ without loss of generality, since the dynamics depend only on the J_{long}/J_z ratio. The light-cone boundary is obtained from first-arrival times, which are the earliest times at which $\|\Delta\rho_n(t)\|_F \geq 0.01$, fitted to a straight line. The outside-the-cone profile is extracted at a fixed time slice by locating the crest of the wave propagating outward from the perturbation and fitting the decay of $\|\Delta\rho_n(t)\|_F$ beyond the wave crest (see insets of Fig. 1).

B. Formal Derivation: Holstein–Primakoff Transformation and Linear Spin Wave Theory

We derive the effective Hamiltonian for the spin model of Eq. (1) using the Holstein–Primakoff (HP) transformation in the linear spin wave approximation, valid in the low-excitation regime. The standard HP transformation assumes a fully $+z$ polarized ferromagnetic vacuum, and the HP mapping reads:

$$\hat{S}_z = S - \hat{n}, \quad (\text{S1})$$

$$\hat{S}_+ = \sqrt{2S} \sqrt{1 - \frac{\hat{n}}{2S}} \hat{a}, \quad (\text{S2})$$

$$\hat{S}_- = \sqrt{2S} \hat{a}^\dagger \sqrt{1 - \frac{\hat{n}}{2S}}, \quad (\text{S3})$$

where the ladder operators are defined as $\hat{S}_\pm = \hat{S}_x \pm i\hat{S}_y = \frac{1}{2}(\sigma_x \pm i\sigma_y)$ and $\hat{n} = \hat{a}^\dagger \hat{a}$.

In the low-excitation (dilute) regime, where $\hat{n} \ll 2S$, the square root can be expanded as a power series:

$$\sqrt{1 - \frac{\hat{n}}{2S}} = 1 - \frac{\hat{n}}{4S} - \frac{\hat{n}^2}{32S^2} - \dots \quad (\text{S4})$$

In the zeroth-order (linearized) approximation of the HP transformation, which keeps only the leading behaviour in $\langle \hat{a}^\dagger \hat{a} \rangle$, the spin operators become $\hat{S}_+^{(0)} = \sqrt{2S} \hat{a}$, $\hat{S}_-^{(0)} = \sqrt{2S} \hat{a}^\dagger$, $\hat{S}_z^{(0)} = S - \hat{a}^\dagger \hat{a}$, and so $\sigma_x \approx \hat{a} + \hat{a}^\dagger$, $\sigma_y \approx i(\hat{a}^\dagger - \hat{a})$, $\sigma_z = 1 - 2\hat{a}^\dagger \hat{a}$.

Note that the terms involving σ^x (i.e., the J_{long} terms) are exact. The hopping terms, on the other hand, are the zeroth-order contributions in the expansion shown in Eq. (S4). However, our model is defined with a ground

state polarized along the x -axis, so we apply a $\pi/2$ rotation about the y -axis, $\hat{R}_y(\frac{\pi}{2}) = e^{-i\frac{\pi}{4}\sigma_y}$. Substituting the linearized HP expressions into the rotated frame gives $\sigma_z \approx -(\hat{a} + \hat{a}^\dagger)$, $\sigma_y \approx i(\hat{a}^\dagger - \hat{a})$, $\sigma_x = 1 - 2\hat{n}$.

Applying the rotated bosonic operators to the Hamiltonian of Eq. (1),

$$\hat{H} = \sum_j J_z \sigma_j^z \sigma_{j+1}^z + \sum_{i < j} \frac{J_x}{|i-j|^\alpha} \sigma_i^x \sigma_j^x, \quad (\text{S5})$$

we obtain:

$$\begin{aligned} \hat{H}^{(0)} = & J_z \sum_j \left(\hat{a}_j^\dagger \hat{a}_{j+1} + \hat{a}_{j+1}^\dagger \hat{a}_j + \hat{a}_j^\dagger \hat{a}_{j+1}^\dagger + \hat{a}_j \hat{a}_{j+1} \right) \\ & - 2 \sum_{i < j} \frac{J_x}{|i-j|^\alpha} (\hat{n}_i + \hat{n}_j) + 4 \sum_{i < j} \frac{J_x}{|i-j|^\alpha} \hat{n}_i \hat{n}_j \\ & + \sum_{i < j} \frac{J_x}{|i-j|^\alpha}. \end{aligned} \quad (\text{S6})$$

Beyond linear order, the HP expansion introduces density-dependent hopping terms $\sqrt{1 - \frac{\hat{n}}{2S}} \approx 1 - \frac{\hat{n}}{4S}$, leading to interaction-assisted hopping, which we denote $\delta\hat{H}^{(1)}$. So

$$\hat{H} = \hat{H}^{(0)} + \delta\hat{H}^{(1)}, \quad (\text{S7})$$

where $\hat{H}^{(0)}$ is given by Eq. (S6), and the additional terms at the next order are:

$$\begin{aligned} \delta\hat{H}^{(1)} = & J_z \sum_{j=1}^{L-1} \left[-\frac{1}{4} (\hat{a}_j + \hat{a}_j^\dagger)(\hat{n}_{j+1} \hat{a}_{j+1} + \hat{a}_{j+1}^\dagger \hat{n}_{j+1}) \right. \\ & -\frac{1}{4} (\hat{n}_j \hat{a}_j + \hat{a}_j^\dagger \hat{n}_j)(\hat{a}_{j+1} + \hat{a}_{j+1}^\dagger) \\ & \left. + \frac{1}{16} (\hat{n}_j \hat{a}_j + \hat{a}_j^\dagger \hat{n}_j)(\hat{n}_{j+1} \hat{a}_{j+1} + \hat{a}_{j+1}^\dagger \hat{n}_{j+1}) \right]. \end{aligned}$$

Since in spin- $\frac{1}{2}$ systems double occupancy is forbidden, every term in $\delta\hat{H}^{(1)}$ necessarily attempts either over-annihilation or creation on an already occupied site, and therefore all such contributions vanish identically in every band. Thus we recover the effective Hamiltonian, Eq. (4).

C. Band Gap and Band Width

For $\alpha = 0$, the long-range interaction reduces to an all-to-all coupling. In this case, the Hamiltonian can be expressed in terms of the collective spin S^x , and the band

energies and energy gaps are given by,

$$E_b = \frac{J_x}{2}(N - 2b)^2 - \frac{J_x N}{2}, \quad (\text{S8})$$

$$\Delta E_b = E_b - E_{b-1} = 2J_x(N - 2b - 1). \quad (\text{S9})$$

Thus the spectrum is quadratic in b , with band gaps linear in b . The largest gap is between $b = 0$ and $b = 1$ (or equivalently between $b = N$ and $b = N - 1$), scaling as $\Delta E \sim 2J_x N$ for large N .

For nonzero α , the gap scales as $\Delta E \sim 2J_x N^{1-\alpha}$. Additionally, the intraband degeneracy is lifted. Taking the $b = 1$ band, a basis state with the k -th spin flipped is $|k\rangle = |+\cdots \underbrace{-}_{k} \cdots +\rangle$.

Each such state is an eigenstate of the long-range term, with energy

$$E_k = E_{b=0} - 2J_x \sum_{j \neq k} \frac{1}{|j - k|^\alpha} = E_0 - 2J_x \epsilon_k, \quad (\text{S10})$$

where the sum over all pairs involving site k is:

$$\epsilon_k = \sum_{s=1}^{k-1} \frac{1}{s^\alpha} + \sum_{s=1}^{N-k} \frac{1}{s^\alpha}. \quad (\text{S11})$$

This defines a smooth external potential ϵ_k . For $\alpha > 1$, the sum converges to the Riemann zeta function, $\epsilon_k \rightarrow 2\zeta(\alpha)$. For $\alpha < 1$, the sum diverges as $\epsilon_k \sim \frac{N^{1-\alpha}}{1-\alpha}$. The largest intraband energy difference (band width) occurs between a spin flip at the chain center and one at the edge, and is given by $2J_x \delta_{\alpha,N}$, where

$$\delta_{\alpha,N} = \epsilon_{N/2} - \epsilon_1 \approx \frac{N^{1-\alpha}}{1-\alpha} (2^\alpha - 1),$$

which for large N and small α behaves as

$$\delta_{\alpha,N} \approx \alpha(\ln 2) N^{1-\alpha}. \quad (\text{S12})$$

Thus, the band width is

$$\delta E_1 \sim 2J_x \delta_{\alpha,N} \sim 2J_x \alpha(\ln 2) N^{1-\alpha}. \quad (\text{S13})$$

Comparing this with the inter-band gap, the ratio for small α is

$$\frac{\delta E_1}{\Delta E_1} \sim \frac{2J_x(\ln 2)\alpha N^{1-\alpha}}{2J_x N^{1-\alpha}} = (\ln 2)\alpha. \quad (\text{S14})$$

As $\alpha \rightarrow 1$, the ratio becomes of order unity. For higher bands, the band width is further enhanced by an extra factor of b , with all b excitations located near the chain center and all b excitations near the edge being the two extreme cases. Therefore, it is sufficient to examine the width of band 1, since the onset of overlap for band 1 implies that all higher bands are already in the overlapping regime.

D. Subspace Projection Derivation of the Effective Hamiltonian

We begin with the single-excitation band ($b = 1$). The nearest-neighbor Ising term induces hopping, giving

$$\hat{H}_{\text{eff}}^{b=1} = J_z \sum_j (|j\rangle\langle j+1| + \text{h.c.}) - 2J_x \sum_j \epsilon_j |j\rangle\langle j|. \quad (\text{S15})$$

Thus the $b = 1$ band maps to a local tight-binding model with position-dependent onsite potential.

For $\alpha < 1$, locality within the $b = 1$ band translates to approximate locality of the full dynamics when the initial state is in this band.

Higher bands. A basis state in band b has b flipped spins, or all spins in a set D flipped. The contribution to the energy from the J_x interaction can be decomposed as

$$\begin{aligned} E &= J_x \sum_{i < j} \frac{s_i s_j}{(j-i)^\alpha} = J_x \left[\sum_{\substack{i < j \\ i, j \notin D}} \frac{1}{(j-i)^\alpha} - \sum_{\substack{i < j \\ i \in D, j \notin D}} \frac{1}{(j-i)^\alpha} - \sum_{\substack{i < j \\ i \notin D, j \in D}} \frac{1}{(j-i)^\alpha} + \sum_{\substack{i < j \\ i, j \in D}} \frac{1}{(j-i)^\alpha} \right] \\ &= J_x \left[\sum_{i < j} \frac{1}{(j-i)^\alpha} - 2 \sum_{j \in D} \sum_{i \neq j} \frac{1}{|j-i|^\alpha} + 4 \sum_{\substack{i, j \in D \\ i < j}} \frac{1}{|j-i|^\alpha} \right] = E_{b=0} + \sum_{j \in D} V(j) + \sum_{\substack{i, j \in D \\ i < j}} W(i, j), \end{aligned} \quad (\text{S16})$$

where

$$E_{b=0} = J_x \sum_{i < j} \frac{1}{(j-i)^\alpha}, \quad V(j) = -2J_x \sum_{i \neq j} \frac{1}{|j-i|^\alpha},$$

and

$$W(i, j) = \frac{4J_x}{|j-i|^\alpha}.$$

Thus, the projected Hamiltonian for band b contains a local onsite potential V and a nonlocal two-body term W .

After Kac rescaling, the one-body potential scales as $O(\alpha J_{\text{long}})$ for small α , while the two-body term is at most $O(b^2 J_{\text{long}}/N^{1-\alpha})$. Hence for $\alpha < 1$, fixed b , and $N \rightarrow \infty$, W becomes negligible and the effective Hamiltonian approaches locality.

Second-quantized form. Introducing creation/annihilation operators $\hat{a}_i^\dagger, \hat{a}_i$ for up spins in the σ_x basis, one finds

$$\hat{V} = \sum_i V(i) \hat{a}_i^\dagger \hat{a}_i + \sum_{i < j} W(i, j) \hat{a}_i^\dagger \hat{a}_i \hat{a}_j^\dagger \hat{a}_j, \quad (\text{S17})$$

with a hard-core constraint forbidding double occupancy. The Ising term provides the kinetic energy

$$\hat{T} = J_z \sum_i \left(\hat{a}_i^\dagger \hat{a}_{i-1} + \hat{a}_{i-1}^\dagger \hat{a}_i \right). \quad (\text{S18})$$

Collecting terms gives the effective Hamiltonian (4), a hard-core Bose–Hubbard model with one-body and two-body potentials. All contributions are local except for W , which vanishes in the limit $N \rightarrow \infty$ for $\alpha < 1$ and fixed b . The second term in Eq. (4) contains the interband couplings.

E. Projecting onto a Single Band

In what follows, \hat{H}_{eff} is the effective Hamiltonian (4), which is equivalent to the full Hamiltonian, and \hat{H}_{eff}^b is the effective Hamiltonian projected on band b (without interband coupling).

Band 1: In Fig. S1, we confirm that the dynamics generated by $\hat{H}_{\text{eff}}^{b=1}$, the Hamiltonian projected onto band 1, with initial states in band 1, generates a perfectly local light cone regardless of the values of α and J_{long}/J_z .

Intraband nonlocality scaling (higher bands): As discussed in the main text, intraband nonlocality appears only at nonzero α . When the dynamics is confined to a single band, a nonlocal light cone is generated at every excitation site. If the excitations are confined in a small region, then outside this region the spread of information is still local, i.e., the signal outside the excitation region decays exponentially with the distance. On the other hand, in the region where excitations are present, nonlocality appears with a well-defined structure determined by the emergence of a nonlocal light-cone around each excitation.

Below, we study the intensity of the signal in the non-local light cones as a function of J_{long}, N , and α . The signal in nonlocal light cones increases with J_{long} (Figs. S2(right), S3) and decreases with N if we use the Kac

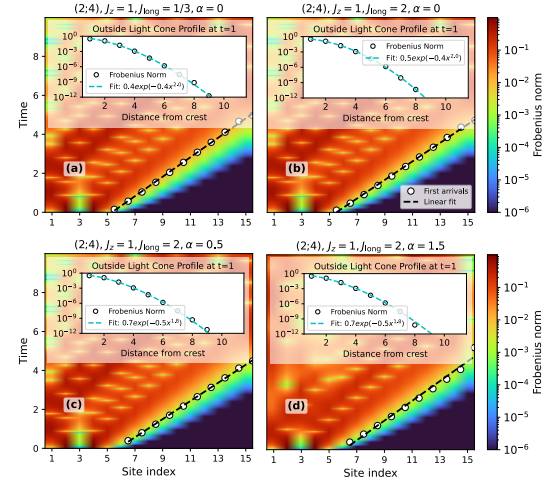


FIG. S1. Density plots of the Frobenius norm showing light-cone dynamics under the projected Hamiltonian $\hat{H}_{\text{eff}}^{b=1}$ with initial states prepared in band $b = 1$: (2; 4) (notation defined in Eq. (9)). (a) $\alpha = 0$ for $J_{\text{long}}/J_z = 1/3$, (b) $\alpha = 0$ for $J_{\text{long}}/J_z = 2$, (c) $\alpha = 0.5$ for $J_{\text{long}}/J_z = 2$, (d) $\alpha = 1.5$ for $J_{\text{long}}/J_z = 2$. For all values of J_{long}/J_z and α , $\hat{H}_{\text{eff}}^{b=1}$ produces a strictly local light cone. White circles mark first arrivals; the black dashed line is the linear fit defining the light-cone velocity (see Supplemental Material A for conventions). Insets show the outside-the-cone profile at $t = 1$.

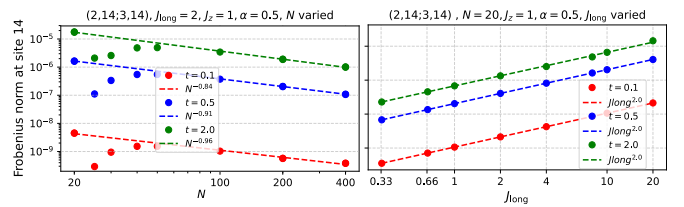


FIG. S2. Frobenius norm at site 14 for $\alpha = 0.5$ under the projected Hamiltonian $\hat{H}_{\text{eff}}^{b=2}$. Left: dependence on system size N for initial state in band 2: (2, 14; 3, 14) (notation defined in Eq. (9)). The intraband nonlocal signal scales as $\sim N^{-1}$ as analytically expected from Eq. (12). The asymptotic scaling is evident for $N \gtrsim 100$. Right: dependence on J_{long} at fixed $N = 20$ for the same initial state, showing $\sim J_{\text{long}}^2$ scaling.

prescription (Fig. S2(left)). Specifically, for $\alpha = 0.5$, the nonlocal signal varies as J_{long}^2/N , consistent with Eq. (12). For given J_{long} and N , the nonlocal signal increases with α , peaking at $\alpha = 1$ (Fig. S4), and decreases nontrivially as the excitations move apart (Fig. S5). Fixing the distance and increasing N , the nonlocal signal decreases in strength (Fig. S6).

F. Truncating to Low-Lying Bands

For moderate to large long-range coupling J_{long} , interband coupling is suppressed. As a result, when the system is initialized in a low-lying band, the ensuing dynamics remain predominantly confined to the low-lying

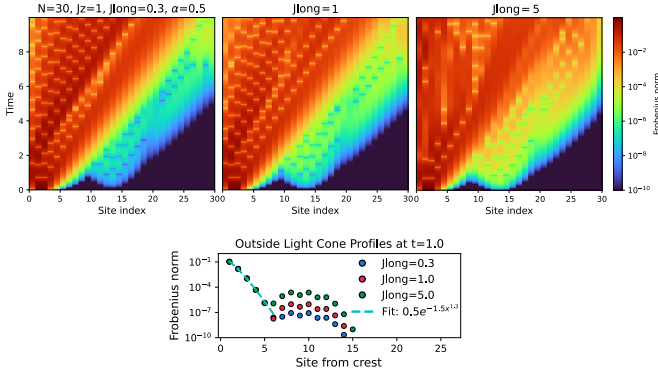


FIG. S3. Density plots of the Frobenius norm showing light-cone dynamics under the projected Hamiltonian $\hat{H}_{\text{eff}}^{b=2}$ with initial states prepared in band $b = 2$: (2,14; 3,14) (notation defined in Eq. (9)). Here $N = 30$ and $\alpha = 0.5$. From left to right, the three panels correspond to $J_{\text{long}} = 0.3, 1, 5$. The lower panel shows the profile of the Frobenius norm outside the light cone at time $t = 1$. Nonlocality gets stronger with increasing J_{long}/J_z , consistent with Eq. (S2).

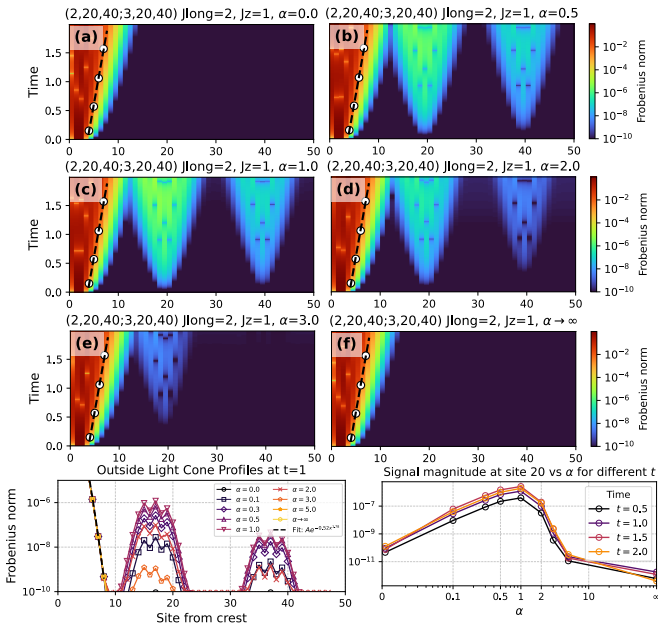


FIG. S4. Density plots of the Frobenius norm showing light-cone dynamics under the projected Hamiltonian $\hat{H}_{\text{eff}}^{b=3}$ with initial states prepared in band 3 (2,20,40; 3,20,40) (notation defined in Eq. (9)) with $J_{\text{long}} = 2$ and $N = 100$ (only 50 sites shown). The six panels differ only in the values of α . For $\alpha=0$ and $\alpha \rightarrow \infty$ (implemented by keeping only nearest-neighbor couplings), the nonlocal signal disappears. The bottom-left panel shows the light-cone profiles at $t = 1$, where the secondary lobes peak at $\alpha = 1$ and weaken for $\alpha > 1$. The bottom-right panel quantifies this by plotting the signal at site $j = 20$ versus α , revealing a maximum at $\alpha = 1$ followed by a decay in the short-range regime $\alpha \gg 1$.

bands. It therefore makes sense to employ an approximation where the Hamiltonian is truncated to low-lying excitation bands; this permits extending the calculation to

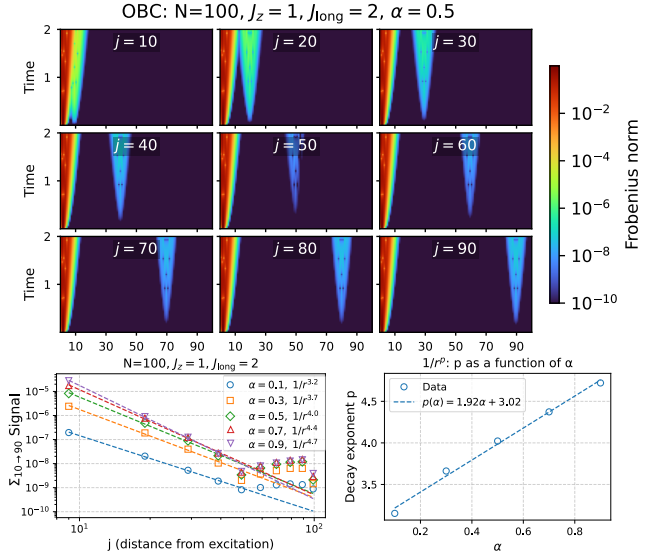


FIG. S5. The nine density plots show the Frobenius norm for initial state $(2, j; 3, j)$, for nine different excitation positions j , evolved by the band 2 projected Hamiltonian $\hat{H}_{\text{eff}}^{b=2}$. The lower left panel shows the summed signal over sites 10–90 at $t = 0.5$ versus j , for $N = 100$, $J_{\text{long}} = 2$, and $\alpha = 0.5$. The dashed lines show $1/r^{p(\alpha)}$ scaling of the signal, with $r = j - 3$, up to mid-chain, beyond which boundary effects appear for open boundary conditions. The lower right panel shows the exponent $p(\alpha)$ for different α values. The exponent increases as $\approx 3 + 2\alpha$ for $t = 0.5$.

larger N , and better exploring the thermodynamic limit, while maintaining computational accuracy. However, truncation introduces artificial nonlocality, even when W is turned off: by restricting the accessible bands, independent distant processes can become artificially correlated. For example, flipping the spin pair (20, 21) or (30, 31) in a band 1 state corresponds to a transition from band 1 to band 3, but flipping both pairs simultaneously would reach band 5. If band 5 is excluded by the truncation, this process is forbidden, and the truncation imposes an unphysical (and nonlocal) constraint. Including higher bands (e.g., band 5 in this case) eliminates these unphysical correlations and restores locality.

Single-band truncations, or projections (e.g., $\hat{H}_{\text{eff}}^{b=1}$, as shown in Fig. S7, or $\hat{H}_{\text{eff}}^{b=3}$, not shown) remain strictly local as shown in the previous section. However, coupling just two bands (e.g., 1 and 3) generates weak nonlocal signals even without explicit long-range terms (see “b3” curve in Fig. S7). Because such truncation-induced effects mask the intrinsic scaling of the nonlocal term, we do not pursue this approach further. Otherwise, this is a promising method to study the asymptotic scaling for $N \rightarrow \infty$.

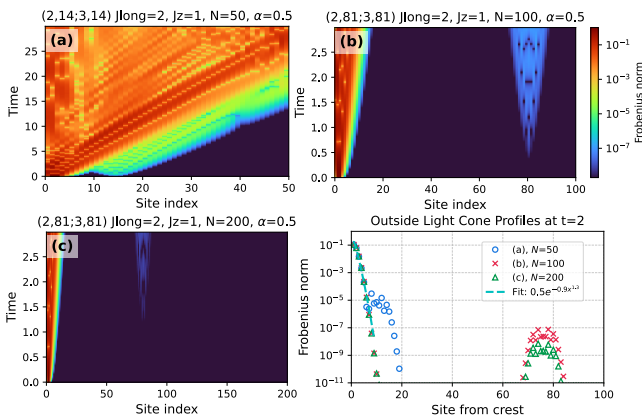


FIG. S6. Panels (a–c) present density plots illustrating light-cone dynamics under the projected Hamiltonian $\hat{H}_{\text{eff}}^{b=2}$ with initial states in band $b = 2$ for $N = 50, 100, 200$, $J_{\text{long}} = 2$, and $\alpha = 0.5$. Panel (d) shows the profile of the Frobenius norm outside the light cone at time $t = 2$. Here nonlocality weakens with increasing N , as seen already in Fig. S2(left), and strengthens when the second excitation lies closer to the first [compare $(2, 14; 3, 14)$ in (a) with $(2, 81; 3, 81)$ in (b,c)], consistent with Eq. (S2).

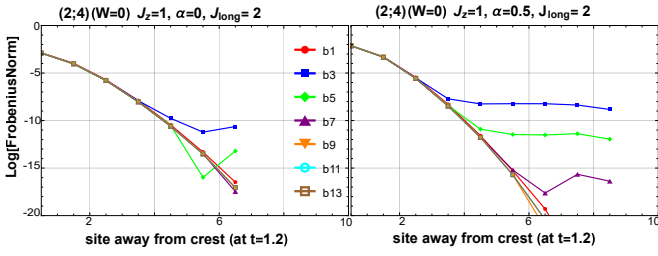


FIG. S7. Decay outside the light cone at a fixed time for different band truncations. We turn off W , so we expect strict locality. Here $N = 13$, $J_{\text{long}} = 2$, and the initial state is $(2; 4)$, in band 1. Here curve b5 illustrates the case where all bands up through band 5 are included in the calculation, and similarly for the other curves. Left: $\alpha = 0$. Right: $\alpha = 0.5$.

G. With and Without W

In order to show that W represents the sole driver of nonlocality, we present in Fig. S8 a direct comparison between evolution under the full Hamiltonian (left column) and the Hamiltonian with the W term subtracted from Eq. (4) (right column), for different values of α and J_{long} . As one can clearly see, setting $W = 0$ restores the local behavior in all cases.

H. Fidelity and Validity of the Effective Hamiltonian

Locality generally emerges in the thermodynamic limit as the nonlocal contribution W vanishes. To test this directly, we compare dynamics generated by the

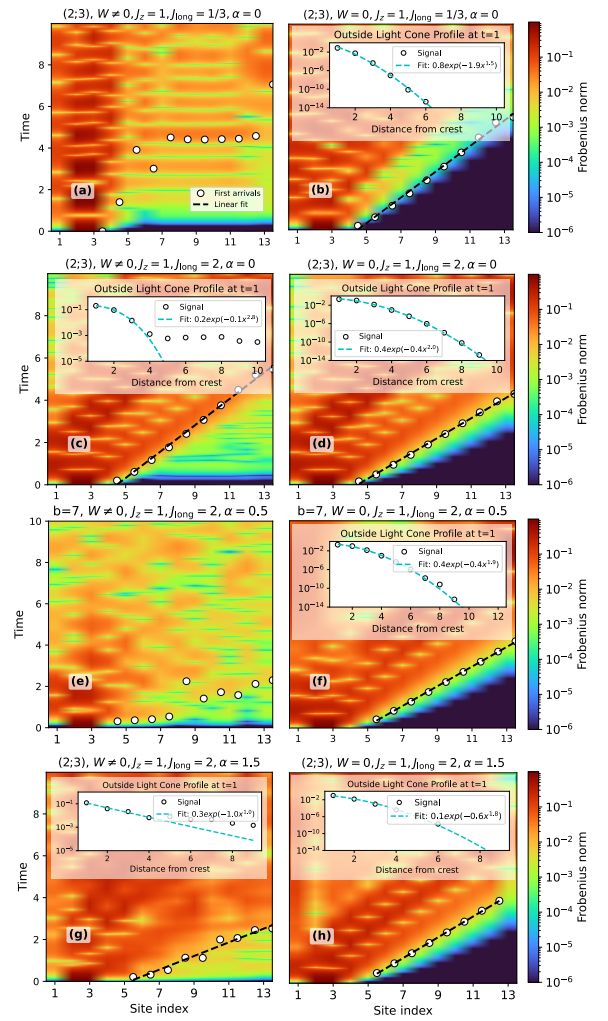


FIG. S8. Density plots of the Frobenius norm showing light-cone dynamics under the full Hamiltonian (1). Setting $W = 0$ (right panel in each row) enforces strict locality even for $J_{\text{long}}/J_z < 1$, for initializations in high-lying bands, and for $1 < \alpha < 3$. The left panel in each row uses the full Hamiltonian. (a,b) Band 1 initialization at $J_{\text{long}}/J_z < 1$: dynamics are nonlocal for the full Hamiltonian but strictly local when $W = 0$. (c,d) Band 1 initialization for $J_{\text{long}}/J_z > 1$, dynamics are quasi-local for the full Hamiltonian and strictly local with $W = 0$. (e,f) Initialization in a high-lying band, band 7, $(2, 10, 11, 12, 13, 14, 15; 3, 10, 11, 12, 13, 14, 15)$, likewise shows nonlocal behavior for the full Hamiltonian and locality when $W = 0$. (g,h) Even when $\alpha = 1.5$ with band 1 initialization, setting W to 0 yields strictly local dynamics. Insets show the outside-the-cone profile at $t = 1$.

full Hamiltonian with those obtained from the projected effective models. We will call shielding “cooperative” when the fidelity between the two different evolutions increases with N at fixed parameters. In what follows, \hat{H}_{eff} is the effective Hamiltonian (4) which is equivalent to the full Hamiltonian, \hat{H}_{eff}^b is the effective Hamiltonian projected on band b (without interband coupling), and $\hat{H}_{\text{eff}W0}^b$ is the Hamiltonian projected on band b with

$W = 0$. Note that the effective Hamiltonian $\hat{H}_{\text{eff}W0}$ (including all bands but with W artificially set to zero) is unphysical: while setting $W = 0$ in Eq. (4) removes the nonlocal contribution, it simultaneously alters the spectrum of the local terms. Consequently, computing the fidelity using a modified $W = 0$ Hamiltonian can be done only with band projection to avoid unphysical results.

Analytic Expectations: For an initial state $|\psi_0\rangle$ in band b , the fidelity between the two Hamiltonians \hat{H}_{eff}^b and $\hat{H}_{\text{eff}W0}^b$, for example, is defined as

$$\mathcal{F}(t) \equiv |\langle \psi_0 | e^{i\hat{H}_{\text{eff}W0}^b t} e^{-i\hat{H}_{\text{eff}}^b t} | \psi_0 \rangle|^2. \quad (\text{S19})$$

At short times, expanding both exponentials to quadratic order in t , we have

$$\mathcal{F}(t) \approx 1 - t^2 \langle W^2 \rangle + t^2 \langle W \rangle^2 = 1 - t^2 \langle \Delta W^2 \rangle. \quad (\text{S20})$$

Thus the short-time fidelity decay is proportional to the variance of W . This remains valid only while the correction term is small, i.e., for times $t \lesssim \frac{1}{\Delta W}$. The scaling of $\langle \Delta W^2 \rangle$ depends strongly on whether or not Kac rescaling is applied. Defining the infidelity as $1 - \mathcal{F}$, one has *without Kac rescaling*:

$$(1 - \mathcal{F})^{\text{intraband}} \sim \langle \Delta W^2 \rangle \sim f(\alpha)g(b)J_x^2, \quad (\text{S21})$$

and with Kac rescaling:

$$(1 - \mathcal{F})^{\text{intraband}} \sim \langle \Delta W^2 \rangle \sim \frac{f(\alpha)g(b)J_{\text{long}}^2}{N^{2(1-\alpha)}}, \quad (\text{S22})$$

where $f(\alpha)$ and $g(b)$ are functions of α and the band index b , as defined in the main text, Eq. (12).

Interband terms are also shown here for completeness. *Without Kac rescaling*:

$$(1 - \mathcal{F})^{\text{interband}} \lesssim J_x^{-2} N^{-4}, \quad (\text{S23})$$

and with Kac rescaling:

$$(1 - \mathcal{F})^{\text{interband}} \lesssim J_{\text{long}}^{-2} N^{-2}. \quad (\text{S24})$$

Band 2 projected dynamics and cooperative effects: The W term vanishes in band 1, so to study the infidelity associated with neglecting the W term we compare the projected Hamiltonians in band 2: $\hat{H}_{\text{eff}}^{b=2}$ (the full Hamiltonian restricted to band 2) and $\hat{H}_{\text{eff}W0}^{b=2}$ (the same, but with the W term subtracted). Fidelity results are summarized in Fig. S9: fidelity decreases with increasing J_{long} , while for fixed J_{long} the fidelity improves with system size N . Without Kac rescaling, fidelity is nearly independent of N , consistent with the scaling of the W term, Eq. (S21). We also test cooperative effects for the full Hamiltonian and get the expected results.

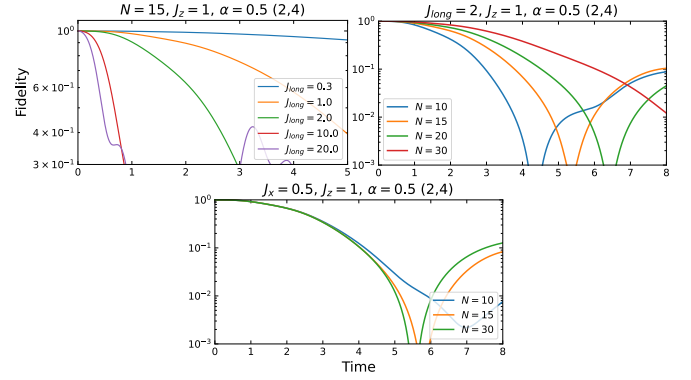


FIG. S9. Fidelity between the band-2 projected Hamiltonian, $\hat{H}_{\text{eff}}^{b=2}$, and the same Hamiltonian with the W term subtracted, $\hat{H}_{\text{eff}W0}^{b=2}$. Left: For $N = 15$, fidelity decreases with increasing J_{long} . Right: For $J_{\text{long}} = 2$, fidelity increases with system size N . Lower panel: For $J_x = 0.5$ (no Kac rescaling), fidelity is independent of N in the regime of high fidelity.

I. Other Physical Observables

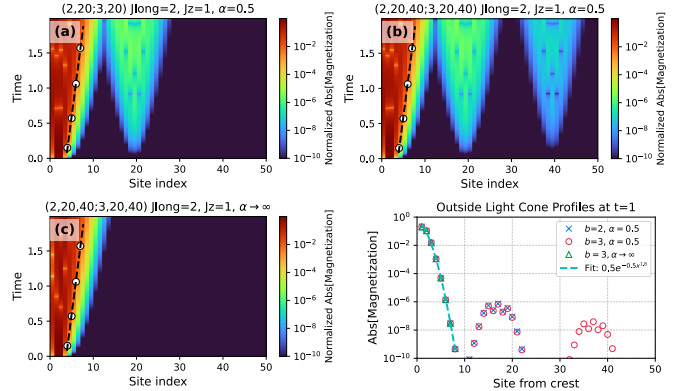


FIG. S10. Light-cone dynamics under the projected Hamiltonian $\hat{H}_{\text{eff}}^{b=2}$ (panel a) and $\hat{H}_{\text{eff}}^{b=3}$ (panels b,c), computed using the site-resolved magnetization, $\left| \frac{\langle \Psi_a | \sigma_n^x | \Psi_a \rangle - \langle \Psi_b | \sigma_n^x | \Psi_b \rangle}{2} \right|$, see Eq. (6), showing that the Frobenius-norm analysis can be reproduced with experimentally accessible observables. This figure reproduces Fig. 6 with magnetization as the observable. $\alpha \rightarrow \infty$ is implemented by keeping only nearest-neighbor couplings.

While our main diagnostic is the Frobenius norm, which is not directly measurable, we show that experimentally accessible quantities, such as the site-resolved magnetization and the connected two-point correlator, exhibit the same qualitative behavior (see Figs. S10 and S11).

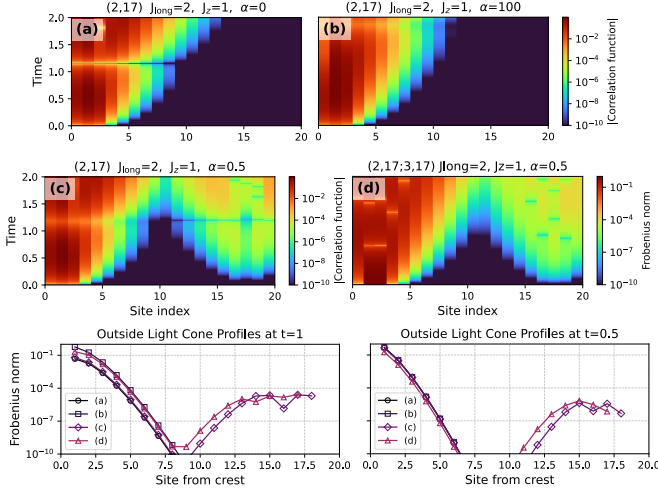


FIG. S11. Panels (a–c): Light-cone dynamics under the projected Hamiltonian $\hat{H}_{\text{eff}}^{b=2}$, computed using the connected two-point correlator $|\langle \sigma_2^x(t) \sigma_j^x(t) \rangle - \langle \sigma_2^x(t) \rangle \langle \sigma_j^x(t) \rangle|$ for the band-2 initial state (2, 17) (notation in Eq. (9)). Panel (d): Frobenius-norm dynamics for the state (2, 17; 3, 17), demonstrating that the Frobenius-norm signatures can be reproduced using experimentally accessible two-point correlations.

J. Nonlocal Light Cones for Different Interaction Ranges

Here we study the emergence of nonlocal light cones for different values of α using the full Hamiltonian, choosing the initial state in band 2. The signal in the nonlocal light cone is highest for $\alpha \approx 1$ and vanishes to numerical precision in the short-range regime $\alpha \rightarrow \infty$ (Fig. S12, panel (f)).

K. Tunable Nonlocality

Figure S13 demonstrates that propagation in this model requires the J_z hopping term, and that the nonlocal light cones arise specifically from the interplay between J_z and the long-range W term. It also shows the extent of control one can have on these systems. In panel (a), where J_z is switched off everywhere, no light-cone structure appears, even in the presence of a B field along z , confirming that the W term alone cannot generate transport – transport requires local coupling J_z . Panels (b–f) show that restoring J_z only in selected spatial regions produces light cones exclusively in those regions,

allowing us to directly control where nonlocal propagation occurs. This establishes that nonlocal light cones originate from the coupling between the W interaction and the band-changing J_z hopping as well as the band-conserving J_z terms. Moreover, by shaping the local profile, the speed and location of the nonlocal light cones can be tuned. Thus, local modulation of J_z provides a practical and experimentally accessible mechanism to engineer

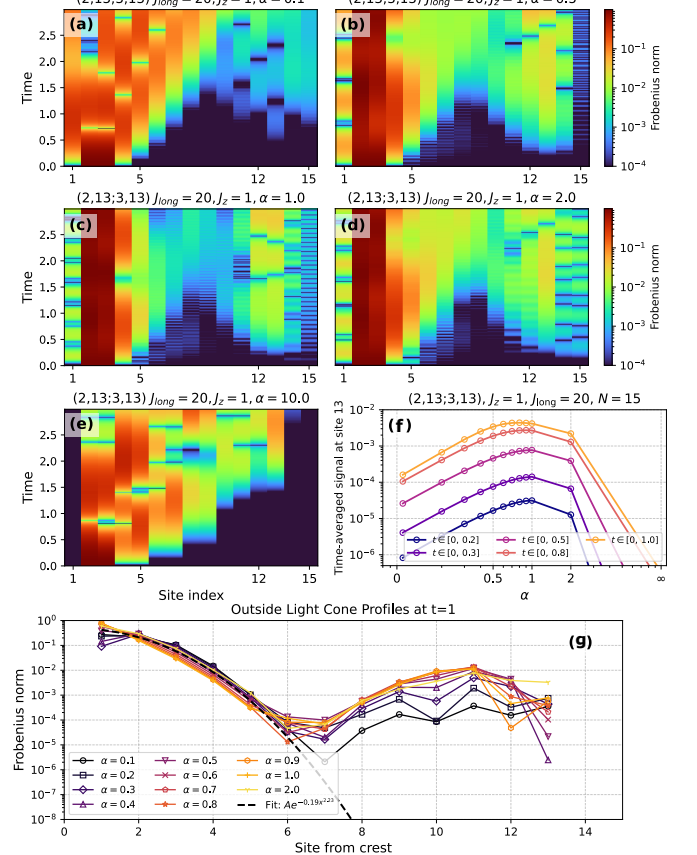


FIG. S12. Panels (a–e): Density plots of the Frobenius norm showing light-cone dynamics under the full Hamiltonian for initial states prepared in band 2, (2, 13; 3, 13) (notation in Eq. (9)). Here $N = 15$ and $J_{\text{long}} = 20$. The nonlocal light cone strengthens as α increases up to $\alpha \leq 1$, and disappears in the short-range limit $\alpha \rightarrow \infty$. Panel (f): Time-averaged Frobenius-norm signal at site $j = 13$ versus α , for different time ranges, showing a peak around $\alpha \approx 1$ and minimal difference between $\alpha = 0.5$ and $\alpha = 1$. Panel (g): Light-cone profiles at $t = 1$ for all α values studied, illustrating the clear nonlocal signal, which should be experimentally observable.

and control nonlocal information transport.

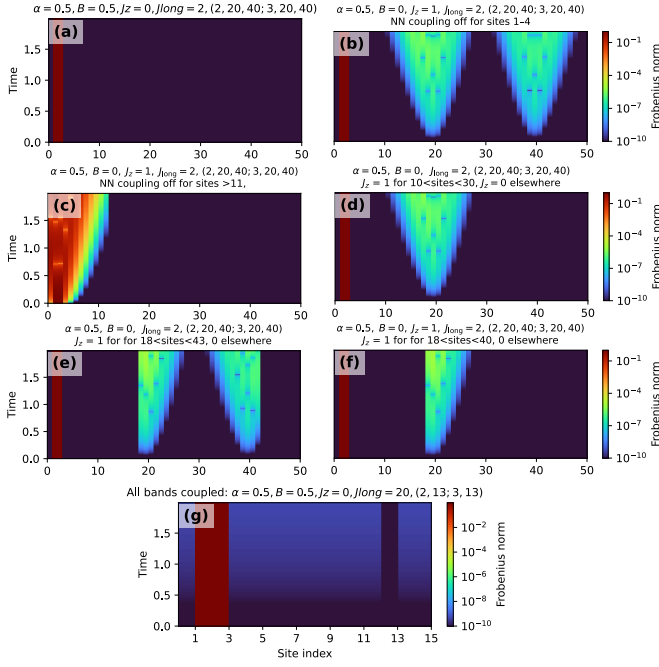


FIG. S13. Density plots of the Frobenius norm showing light-cone dynamics under the band-3-projected Hamiltonian $\hat{H}_{\text{eff}}^{b=3}$ for the initial state $(2, 20, 40; 3, 20, 40)$ [Eq. (9)] with $N = 50$, $J_{\text{long}} = 2$, and $\alpha = 0.5$. (a) B - J_{long} model with an additional longitudinal field term $B \sum_i \sigma_i^z$ with $J_z = 0$. (b–f) Hamiltonian with J_z selectively disabled: (b) $J_z = 0$ on sites 1–4 and $J_z = 1$ elsewhere; (c) $J_z = 0$ for sites > 11 and $J_z = 1$ elsewhere; (d) $J_z = 1$ only in the region of the second light cone; (e) $J_z = 1$ on sites 19–42; (f) same as (e) but excluding site 40. (g) Full Hamiltonian corresponding to panel (a).